



Size measurement of blasted rock fragments based on FRRSnet+

Qinpeng Guo ^{*}, Shijiao Yang ^{*}, Yuchen Wang, Huanbao Zhang

School of Resources Environment and Safety Engineering, University of South China, Hengyang 421000, China

ARTICLE INFO

Keywords:
Blasted rock
Model size
FRRSnet+
Distance transform

ABSTRACT

To accurately segment rock particles in the blasted rock pile image, this study proposes a new segmentation method based on fully residual rock segmentation network plus (FRRSnet +), where FRRSnet + is a new deep learning network proposed by fusing U-net, ResNet, and ASPP. The method consists of two models, FRRSnet + -1 and FRRSnet + -2, where FRRSnet + -1 is responsible for segmenting rocks and background, and FRRSnet + -2 is responsible for complementing the rock edge of FRRSnet + -1 result. Compared with U-net and Segnet showed that better results were obtained by directly using FRRSnet + -1, which had *MRE*, *RMSE*, and *R*² of 2.5%, 1.55, and 99.58%, respectively. More, after using the proposed segmentation method, the segmentation results can be reduced by 1.54% and 0.77% for *MRE* and *RMSE*, respectively, improved by 0.31% for *R*² compared with the results of directly using FRRSnet + -1. The proposed network and segmentation method can provide a more accurate guidance for blast parameter optimization.

1. Introduction

In modern mineral exploitation, blasting cost occupies a large proportion of the overall mineral exploitation cost, resulting in obtaining a good blasting effect, particularly a good blasted rock fragment sizes cumulative distribution, which is essential in the entire mineral exploitation process [1,2]. The blasted rock fragment sizes cumulative distribution is mainly influenced by blasting parameters and geological circumstances. Therefore, it is necessary to collect the rock fragment sizes in the actual field to optimize the blasting parameters to achieve the purpose of reducing blasting costs [3,4]. However, the current measurement of rock fragment sizes is inaccurate, resulting in problems with the optimization model [5–7], which in turn leads to difficulties in achieving the required rock fragment sizes after blasting with the blasting design parameters obtained from the optimization model. Therefore, it is of great engineering significance and practical value to establish an accurate blasted rock pile image (BRPI) segmentation method to obtain blasted rock fragment sizes.

So far, the image segmentation method is the most popular method to obtain the rock size from the BRPI. The cumulative distribution of blasted rock fragment size formed by this method is the closest to the sieving result [8–13]. There are three main challenges in BRPI segmentation: ① blasted rocks have an irregular shape and a significant size difference; ② blasted rocks are severely stacked; ③ rocks have subtle grayscale differences and complex surface texture. Among them, due to

the slight difference in rock grayscale and severe stacking, the rock edges are blurred and difficult to identify accurately [14]. Worse still, the complex surface texture of rocks leads to more “false edges” in the segmentation results obtained using traditional image processing techniques [15–17]. Although Guo et al. [18] proposed an adaptive watershed segmentation algorithm for BRPI based on rock shape, which improved the rock segmentation accuracy to a certain level. However, the complexity of rock shapes is increased by the severe stacking of rocks, which leads to the results obtained using the segmentation method proposed by Guo et al. [18] still having more false segmentation phenomena.

Nowadays, deep learning [19] has become a state-of-the-art technique for performing computer vision tasks such as image classification [20–22], object localization [23], and segmentation [24]. Deep learning is also widely used for rock particle segmentation and detection, and the results obtained by this method are far more accurate than those of traditional image processing techniques [25–27]. The deep learning used for BRPI segmentation is mainly semantic segmentation and instance segmentation [24,25]. However, fewer application studies use deep learning for actual BRPI segmentation due to the limitation of the data set. The semantic segmentation functions by assigning a category to each pixel in the image [28]. Thus, in the labeled images of the BRPI dataset used to train the semantic segmentation network, the rocks are one category, and the parts of the image other than the rocks are another category, which is called the background [26]. However, there is no

* Corresponding authors.

E-mail addresses: 1516682242@qq.com (Q. Guo), 649292197@qq.com (S. Yang).

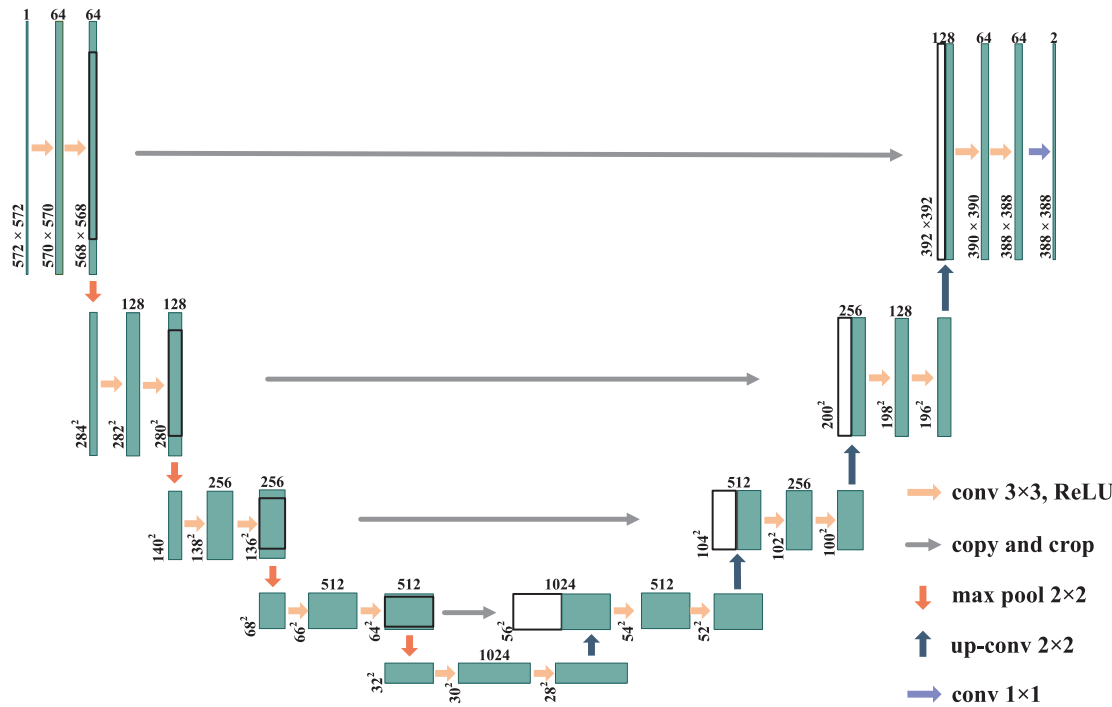


Fig. 1. U-net architecture.

background between rocks stacked on top of each other, so the researchers used a line of 1-pixel width to separate this type of rocks in the labeled images, and the category of this line is background [29,30]. The semantic segmentation network is used to segment BRPI can avoid the influence of difficulties ① and ③. However, it is difficult for the semantic segmentation network to accurately predict the separation lines between rocks due to the stacking of rocks on top of each other, which results in non-existent or discontinuous rock edges [30,31]. Therefore the prediction results of semantic segmentation networks require post-processing by traditional image processing techniques, such as the watershed algorithm [18]. Unlike semantic segmentation, instance segmentation can segment different objects of the same category [32]. Instance segmentation segments rocks by labeling them with various colors [33], so it can avoid the three main difficulties of BRPI segmentation. Shrivastava et al. [34] used Mask R-CNN for segmenting BRPI, which is an instance segmentation network. In their study, Mask R-CNN can achieve excellent results with a percentage error of 1.274 mm and a standard deviation of 0.439 mm. Their study also shows that Mask R-CNN can segment a large range of rock particles from 5 mm to the maximum size in the BRPI. However, as stated by Shrivastava et al. [34] in their study, there is a significant drawback of using the instance segmentation method: the instance segmentation does not identify all the rock particles in the BRPI. In summary, the main reason for the error in the rock segmentation results obtained by the semantic segmentation networks is the non-existence or discontinuity of rock edges, and this problem can be solved by traditional image processing techniques. The main reason for the error in rock segmentation results obtained by the instance segmentation network is that some rock particles are unidentified. More importantly, the size distribution of unidentified rock particles is unknown, which will lead to high uncertainty in the results of the instance segmentation.

The main goal of this study is to establish a method based on deep learning for segmenting BRPI. Two requirements need to be met for this purpose: ① the deep learning network model size is as small as possible to facilitate practical applications, and ② the segmentation accuracy of BRPI is as high as possible. To this end, this study proposes a semantic segmentation network for BRPI segmentation, named fully residual rock segmentation network plus (FRRSnet +). In addition, this study also

proposes a BRPI segmentation method based on semantic segmentation to solve the problem of non-existent or discontinuous rock edges.

To summarize, the major contributions of this study are: ① FRRSnet+, a novel deep learning network for segmenting rocks and backgrounds in images, which mainly features high segmentation accuracy and a small network model size; ② a method based on semantic segmentation for segmenting BRPI, which can solve the problems when semantic segmentation is used for rock segmentation and improve rock segmentation accuracy; ③ a dataset for training FRRSnet+, which contains 14,628 BRPI from open-pit mines, and the images are collected by UAV.

2. Related work

2.1. U-net

U-net [35], a segmentation network for medical imaging, won the ISBI cell tracking challenge in 2015 by a large margin. As shown in Fig. 1, the network is composed of two parts: the contracting path and the expansive path, and these two parts are connected by two 3×3 convolutions. The contracting path is composed of two 3×3 convolutions and a 2×2 max pooling operation, both of which are repeatedly applied four times. The max pooling operation has a step size of 2 and is used for downsampling. The convolution following each max pooling operation doubles the channel number of the feature map. The expanded path is composed of one convolution for upsampling and two 3×3 convolutions, both of which are reused four times. The upsampling process doubles the size of the feature map and halves the number of feature channels. The upsampled feature map is concatenated with the corresponding feature map in the contracting path. After the expanded path is completed, each component feature vector is mapped to a different class using a 1×1 convolution to achieve prediction for each pixel. It should be noted that each convolution is followed by a Batch Normalization (BN) and a rectified linear unit (ReLU). After each completed iteration, the prediction result map is compared with the labeled result map to calculate the pixel-level error, and end-to-end learning is performed by back-propagating this error.

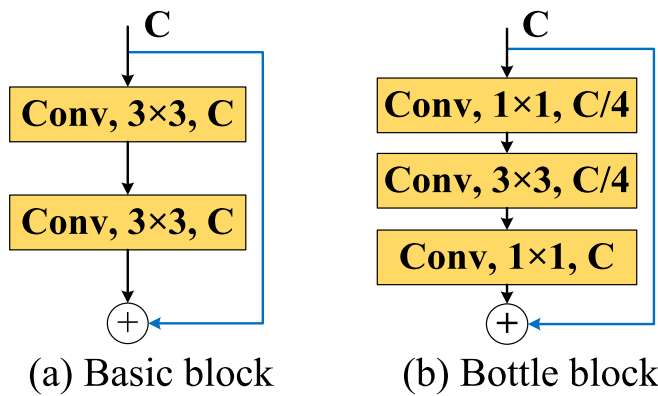


Fig. 2. Residual block. C is the number of channels.

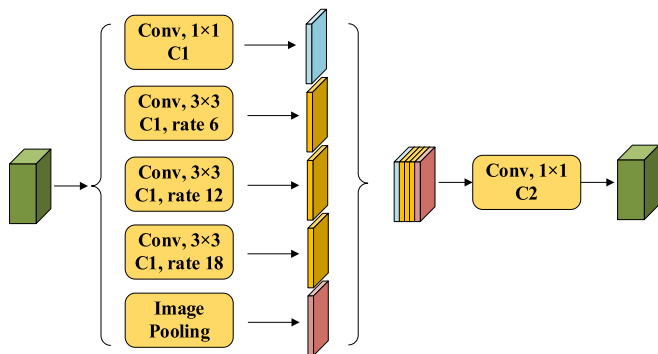


Fig. 3. ASPP architecture. C1 and C2 are the numbers of channels.

2.2. Residual block

To solve the degradation problem in deep network training, He et al. [36] proposed two residual blocks, which are based on the assumption that it is easier to optimize residual mapping than the original and unreferenced mapping. They used these two residual blocks to construct ResNet of different depths, and the network won 1st place on the tasks of ImageNet detection, ImageNet localization, COCO detection, and COCO segmentation in 2015. The architecture of residual blocks is shown in

Fig. 2, where (a) is a basic block for forming ResNet-18 and ResNet-34, (b) is a bottle block for forming ResNet-50, ResNet-101, and ResNet-152. Each convolution in the residual block is followed by a BN and a ReLU. Compared to general convolution, the residual block has identity mapping (blue line in Fig. 2), which effectively alleviates the gradient disappearance problem caused by increasing depth in deep learning networks.

2.3. Atrous spatial pyramid pooling

Atrous spatial pyramid pooling (ASPP) [37] is a module, which is composed of atrous convolution and spatial pyramid pooling structure. The ASPP extracts image multiscale information using atrous convolution with different atrous rates, and obtains the image global information using global average pooling. Finally, the obtained multiscale information and global information are converged using 1×1 convolution. The ASPP module overcomes the drawbacks of local information loss and long-distance information lack of correlation, and the drawbacks are caused by the grid effect when using a single atrous convolution. Moreover, by using atrous convolution, ASPP can obtain different scale feature information without using a pooling operation. The ASPP architecture is shown in Fig. 3.

3. Methods

3.1. Basic network

To achieve the purpose of this study, a basic network similar to the U-net was constructed. The role of this network is to explore the relationship between the network model size and the prediction accuracy of BRPI, and then to determine the appropriate network model size. As shown in Fig. 4, the basic network is composed of two parts: the contracting path and the expansive path, which are connected using two 3×3 convolutions. In the contracting path, a 3×3 convolution is first used for the BRPI, which extracts rich information from the image and expands the channel number of the image to C. Then, the extracted information is processed by two 3×3 convolutions and one convolution for downsampling, and the process is repeated four times. After the BRPI is processed by the contracting path, the image size becomes $16C \times 32 \times 32$. In the expansive path, the image is processed by one 3×3 deconvolution and two 3×3 convolutions, and the process is repeated four times. Finally, each component feature vector is mapped to a

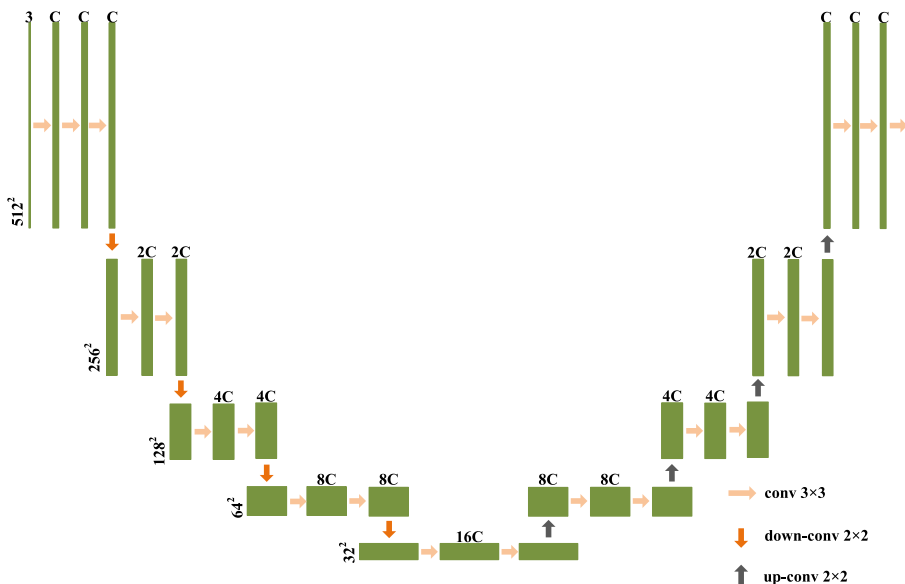


Fig. 4. Basic network architecture. C is the number of channels.

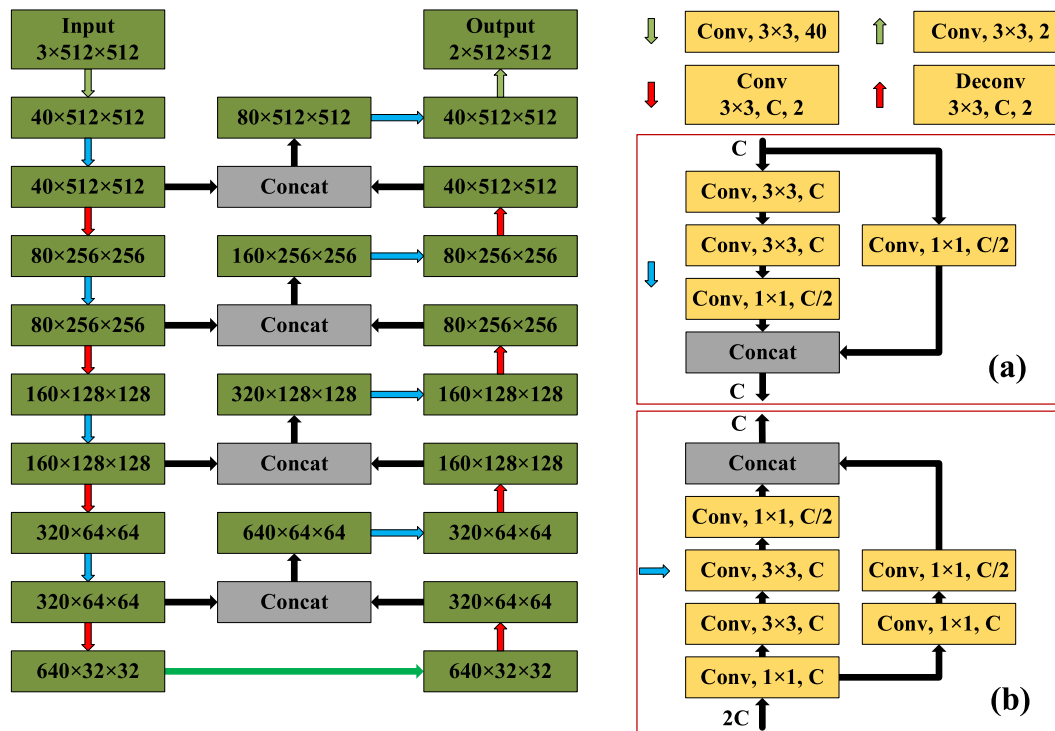


Fig. 5. FCRSnet architecture.

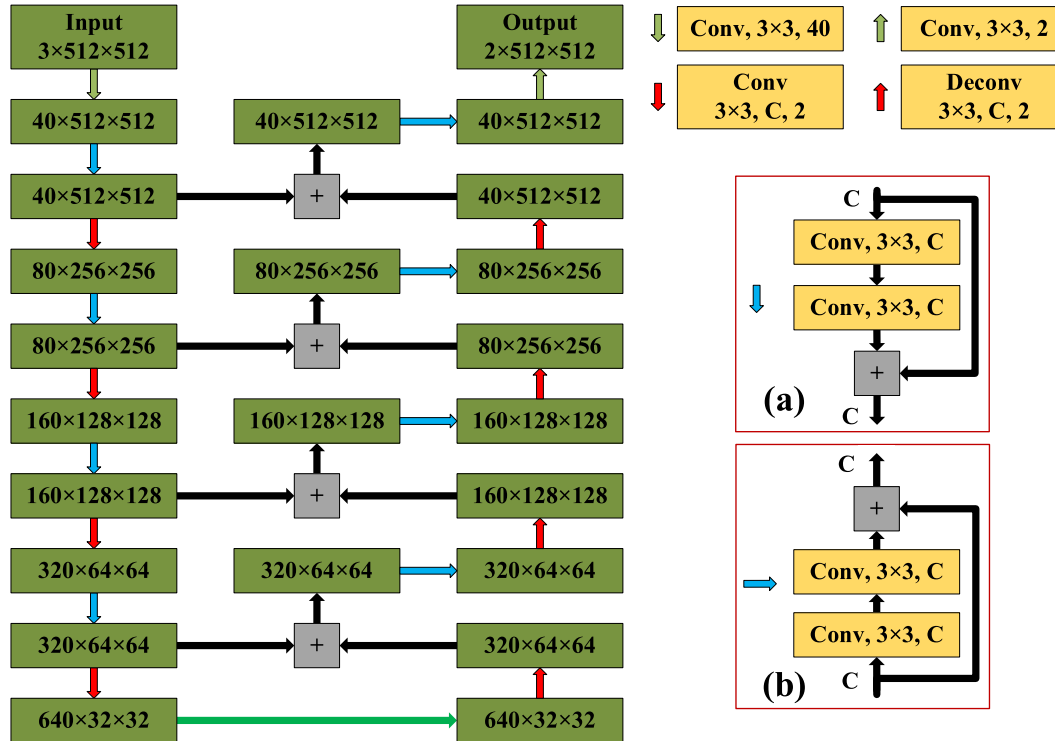


Fig. 6. FRRSnet and FRRSnet + architecture.

different class using one 3×3 convolution.

3.2. FCRSnet

After determining the appropriate model size, skip architecture is used in this study to improve the basic network. The role of skip

architecture is to combine semantic information from a deep, coarse layer with appearance information from a shallow, fine layer to produce accurate and detailed segmentations. The improved network is named the fully concatenation rock segmentation network (FCRSnet), as shown in Fig. 5. The FCRSnet differs from the basic network in four parts: ① the two 3×3 convolutions in the contracting path is replaced by Fig. 5(a);

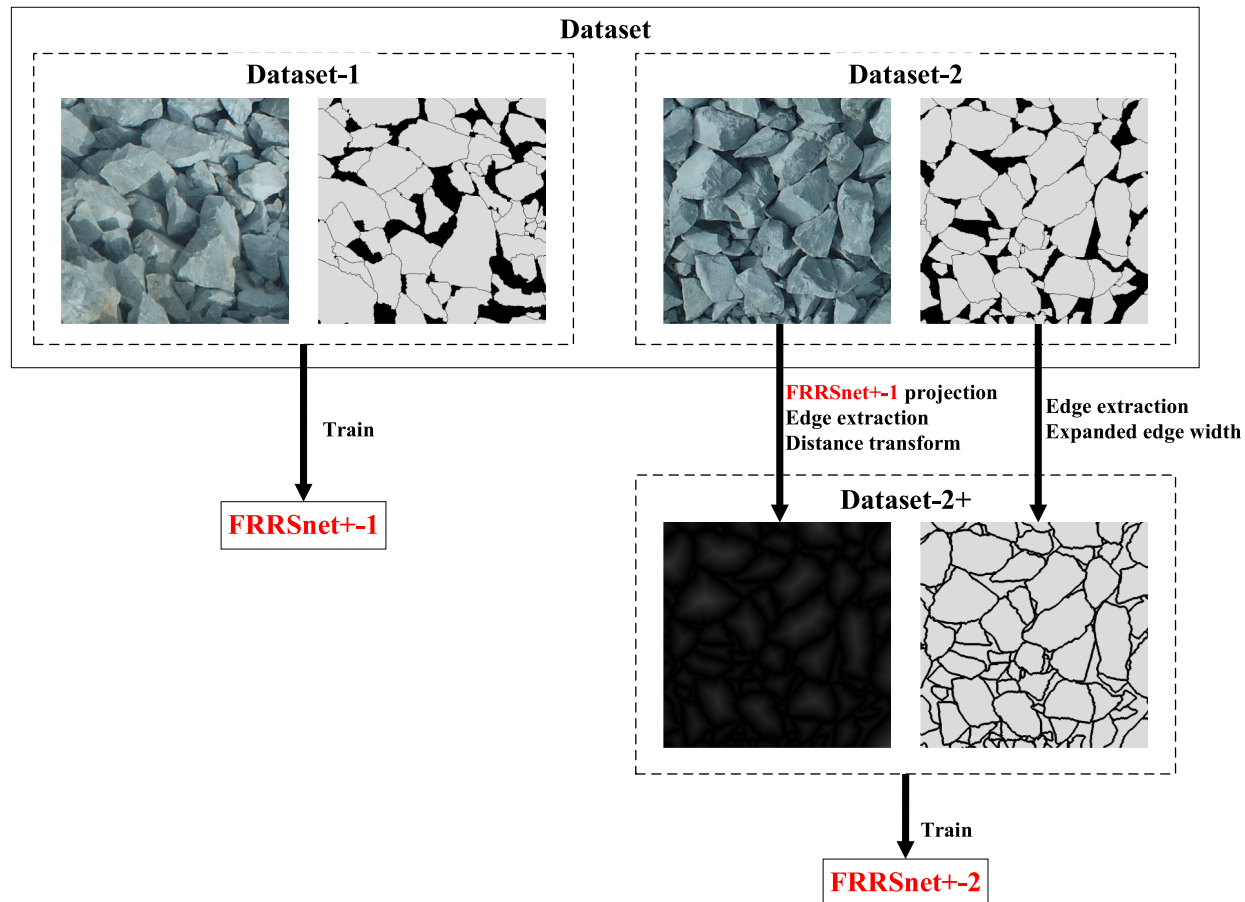


Fig. 7. The model development process.

② the two 3×3 convolutions in the expansive path is replaced by Fig. 5(b); ③ the two 3×3 convolutions used to connect the contracting path and the expansive path is replaced by Fig. 5(a), that is the green arrow in Fig. 5; ④ the skip architecture is added between the contracting path and the expansive path, which connects the corresponding feature map of the contracting path and the expansive path. The 1×1 convolution in Fig. 5(a) and (b) is used to half the channel number and thus avoid increasing the model size.

3.3. FRRSnet and FRRSnet+

In this study, the identity mapping of the residual block is also used to improve the basic network. The improved network is named fully residual rock segmentation network (FRRSnet), as shown in Fig. 6. There are also four differences between the FRRSnet and the basic network: ① the two 3×3 convolutions in the contracting path is replaced by Fig. 6(a); ② the two 3×3 convolutions in the expansive path is replaced by Fig. 6(b); ③ the two 3×3 convolutions used to connect the contracting path and the expansive path is replaced by Fig. 6(a), that is the green arrow in Fig. 6; ④ the identity mapping is added between the contracting path and the expansive path, which adds up the corresponding feature map of the contracting path and the expansive path. Since the identity mapping does not increase the channel number of the feature map, it is not necessary to increase the 1×1 convolution to change the channel number of the feature map in Fig. 6(a) and (b).

In addition, this study also improved the FRRSnet by replacing the module used to connect the contracting path and the expansive path with ASPP, resulting in a new network called fully residual rock segmentation network plus (FRRSnet+), where C1 and C2 of ASPP are 160 and 640, respectively. In order to unchanged the model size of

FRRSnet+, the 1×1 convolution used to fuse the information in ASPP is replaced by a 3×3 convolution.

3.4. Segmentation method of BRPI based on semantic segmentation

It should be noted that for a better description of the BRPI segmentation method, FRRSnet+ is used as an example in this study to introduce this method. This method is divided into two processes: model development and application, with two different models, FRRSnet+ -1 and FRRSnet+ -2, at the core. Where FRRSnet+ -1 is responsible for segmenting the rocks and background, and FRRSnet+ -2 is responsible for supplementing the rock edge information of the FRRSnet+ -1 segmentation result. The model development process of the BRPI segmentation method is as follows:

- (1) The dataset is divided randomly and equally into two groups, dataset-1 and dataset-2, respectively.
- (2) The FRRSnet+ -1 model is obtained by training FRRSnet+ using dataset-1.
- (3) The prediction results are obtained by using FRRSnet+ -1 to predict the input images of dataset-2.
- (4) The edges of the prediction results are extracted, then the extracted edge images are processed using the distance transform to obtain the distance-transformed images.
- (5) The edges in the labeled image of dataset-2 are extracted and widened to 5 pixels. The widened edges images and the distance-transformed images obtained in step (4) then form a new dataset, which is called dataset-2+.
- (6) The FRRSnet+ -2 model is obtained by training FRRSnet+ using dataset-2+.

Table 1
Model training parameters.

Model	Initial weights [38]	Optimization algorithm	Learning rate	Epochs	Batch size	MIoU (%)	Model size (MB)
Basic network-32	Kaiming	Adam	10^{-5}	100	16	95.93	42.0
Basic network-40	Kaiming	Adam	10^{-5}	100	16	97.67	65.6
Basic network-48	Kaiming	Adam	10^{-5}	100	16	98.78	94.4
FCRSnet-1	Kaiming	Adam	10^{-5}	100	10	98.65	70.3
FCRSnet-2	Kaiming	Adam	10^{-5}	100	10	98.02	70.3
FRRSnet-1	Kaiming	Adam	10^{-5}	100	18	98.88	65.6
FRRSnet-2	Kaiming	Adam	10^{-5}	100	18	96.98	65.6
FRRSnet + -1	Kaiming	Adam	10^{-5}	100	18	98.67	66.4
FRRSnet + -2	Kaiming	Adam	10^{-5}	100	18	98.62	66.4
U-net	Kaiming	Adam	10^{-5}	100	10	99.86	131
Segnet	Pre-trained	Adam	10^{-5}	100	20	98.21	112

The application process of the BRPI segmentation method is as follows:

- (1) The segmented image-1 is obtained by predicting the test image using the FRRSnet + -1 model.
- (2) The edges of segmented image-1 are extracted, and then the extracted edge image is processed using the distance transform to obtain the distance-transformed image of segmented image-1.
- (3) The segmented image-2 is obtained by predicting the distance-transformed image using the FRRSnet + -2 model.
- (4) The segmented image-2 and segmented image-1 are overlapped, and the overlapped image is denoted as image-3.
- (5) The preliminary segmented image is obtained by segmenting image-3 using the watershed algorithm.
- (6) The preliminary segmented image is used as the seed point of the watershed algorithm, and the final segmentation result is obtained by applying watershed segmentation to segmented image-1.

4. Data set

4.1. Image acquisition

In this study, the data was collected using the DJI Phantom 4 RTK UAV from two different quarries in Huizhou, China. Most of the acquisition operations were conducted at noon, and the camera was perpendicular to the rock pile surface so that the acquired images were less shaded. As shown in Fig. 9, the rocks in the image have different colors and significant differences in particle size. Moreover, the rocks are stacked on each other, which is the main reason for the false segmentation.

4.2. Labeled image

The quality of the dataset is one of the important factors in determining the performance of the network model. To obtain a high-quality dataset, the collected images were manually labeled in this study, and the labeled image is shown in Fig. 7. The manual labeling follows the following principles:

- (1). The particles with clear surfaces and edges in the image are labeled.

- (2). When particles are stacked on each other, the upper particle is labeled completely, and the lower particle are labeled only for the part of the image that can be seen.
- (3). When all or part of the particle is located in the shaded area, only the visible part is labeled.
- (4). The dust particles were not labeled.

4.3. Train set and test image

A patch of size 512×512 is extracted from the BRPI as the input image, and the corresponding patch is extracted from the labeled image as the output image, thus the training set is formed. The more training data, the better result of the deep learning network, so data augmentation is performed on the original image: ① the original image is rotated before extracting patches; ② a patch of size 512×512 is extracted every 128-pixel interval, the neighboring patches have 75% overlap. After data augmentation, a total of 14,628 input images and their corresponding output images are included in the training set. The images in the test set are two complete images, which are shown in Fig. 9(a) and (b) with sizes of 2304×2016 and 1408×2080 , respectively.

According to the model development process of the BRPI segmentation method proposed in this study, the 14,628 data are randomly and equally divided into two groups, each group contains 7,314 data, which are noted as dataset-1 and dataset-2, as shown in Fig. 7. The dataset-1 is used directly for training FRRSnet + without any processing. The dataset-2 needs to be further processed as shown in Fig. 7, thus forming dataset-2 +.

5. Training and performance comparison

5.1. Determine model size

From Fig. 4, the model size of the basic network is related to channel number C. This study sets three different C, C = 32, 40, and 48, and the formed networks are noted as basic network-32, basic network-40, and basic network-48. The basic network is written using PyTorch 1.9.0 deep learning library in Python 3.8 language and trained using RTX3090 GPU with 24 GB video memory. Detailed training parameters for the basic networks are shown in Table 1. It should be noted that the basic network is trained by dataset-1 and tested by dataset-2 in this study. The dataset-2 contains 7314 data, so the result obtained by testing the three basic networks using this dataset is very convincing.

In this study, two indicators, mean intersection over union (MIoU) and accuracy, are used to evaluate the three base networks, where MIoU

Table 2
Models performance.

Model	Basic network-32	Basic network-40	Basic network-48	FCRSnet	FRRSnet	FRRSnet+
MIoU (%)	94.38	96.09	97.13	96.86	97.56	97.27
Accuracy (%)	98.20	98.77	99.10	99.02	99.24	99.15

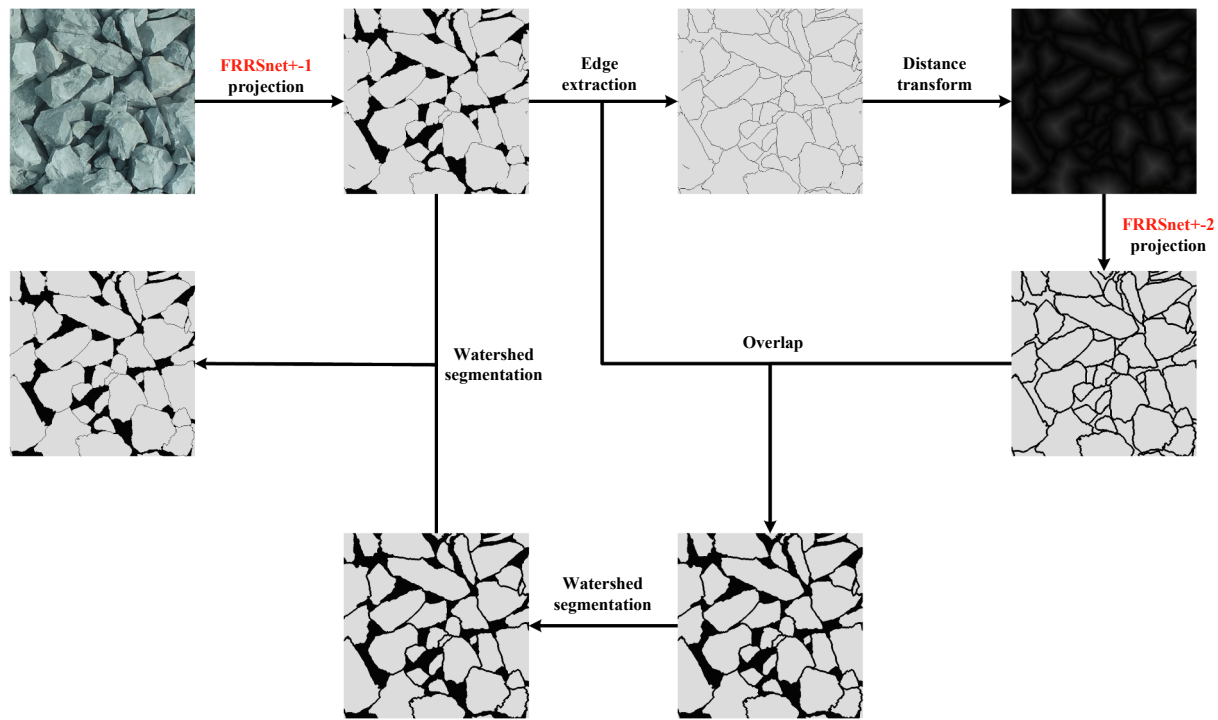


Fig. 8. The application process.

is also used as an indicator to evaluate the training process. The maximum MIoU of the training process is shown in Table 1, and the model size obtained after training is shown in Table 1. It should be noted that MIoU is a standard indicator for semantic segmentation, and the calculation method is shown in Equation (1). The calculation results of two evaluation indicators are shown in Table 2.

$$MIoU = \frac{1}{k} \sum_{i=1}^k \frac{p_{ii}}{\sum_{j=1}^k p_{ij} + \sum_{j=1}^k p_{ji} - p_{ii}} \quad (1)$$

Where k is the number of categories in the labeled image, p_{ii} is the number of pixel points that is predicting i as i , p_{ij} is the number of pixel points that are predicting i as j , and p_{ji} is the number of pixel points that are predicting j as i . There are only two categories in dataset-a and dataset-b in this study, so $k = 2$.

From Table 1, we can see that the MIoU and model size increase as channel number C increases, indicating that the larger the model size,

the better the learning ability of the model. From Table 2, compared to the basic network-32, the basic network-40 increases by 1.71% and 0.57% in MIoU and accuracy indicators, respectively. Compared to the basic network-40, the basic network-48 increases by 1.04% and 0.33% in MIoU and accuracy indicators, respectively. Therefore, this study determines the channel number $C = 40$.

5.2. Training model

According to the two model development processes in Fig. 7, FCRSnet, FRRSnet, and FRRSnet + are trained using datasets, and two models are obtained for each network, resulting in a total of six models, namely FCRSnet-1, FCRSnet-2, FRRSnet-1, FRRSnet-2, FRRSnet + -1, and FRRSnet + -2. All networks are written using the PyTorch 1.9.0 deep learning library in Python 3.8 language and trained using an RTX3090 GPU with 24 GB of video memory. It should be noted that in the 7,314

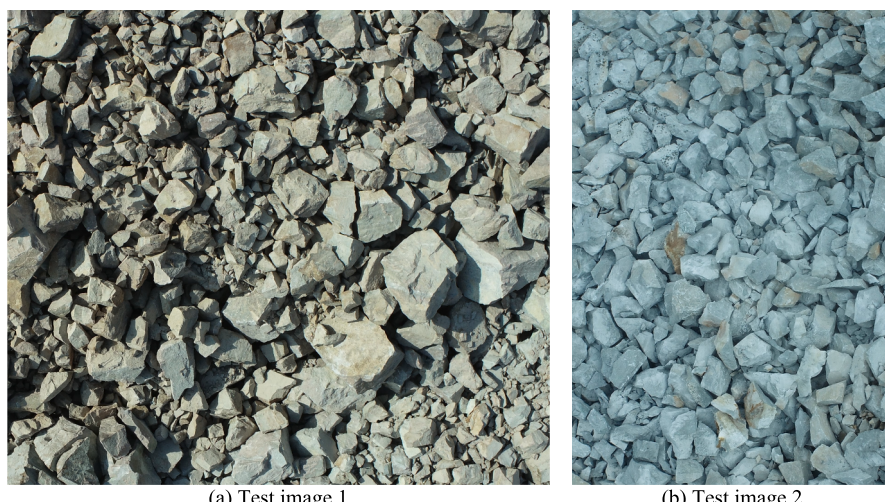


Fig. 9. Test image.

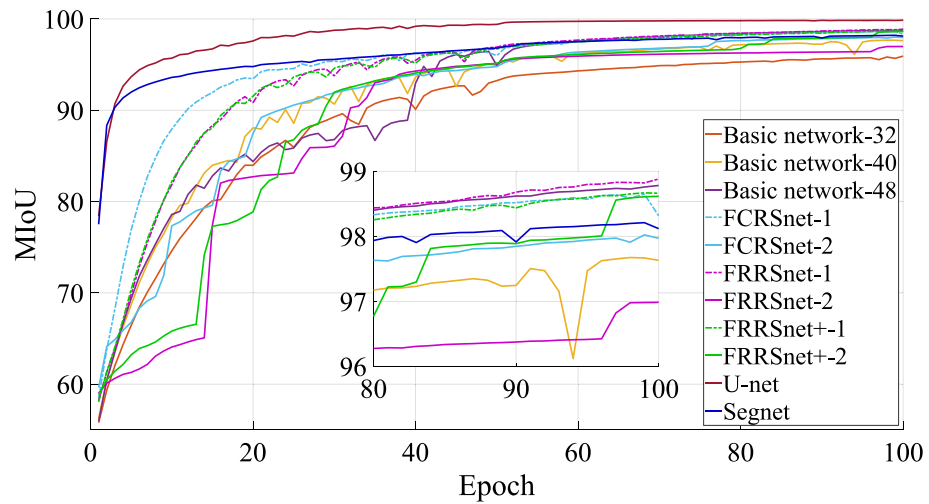


Fig. 10. MIoU for each epoch.

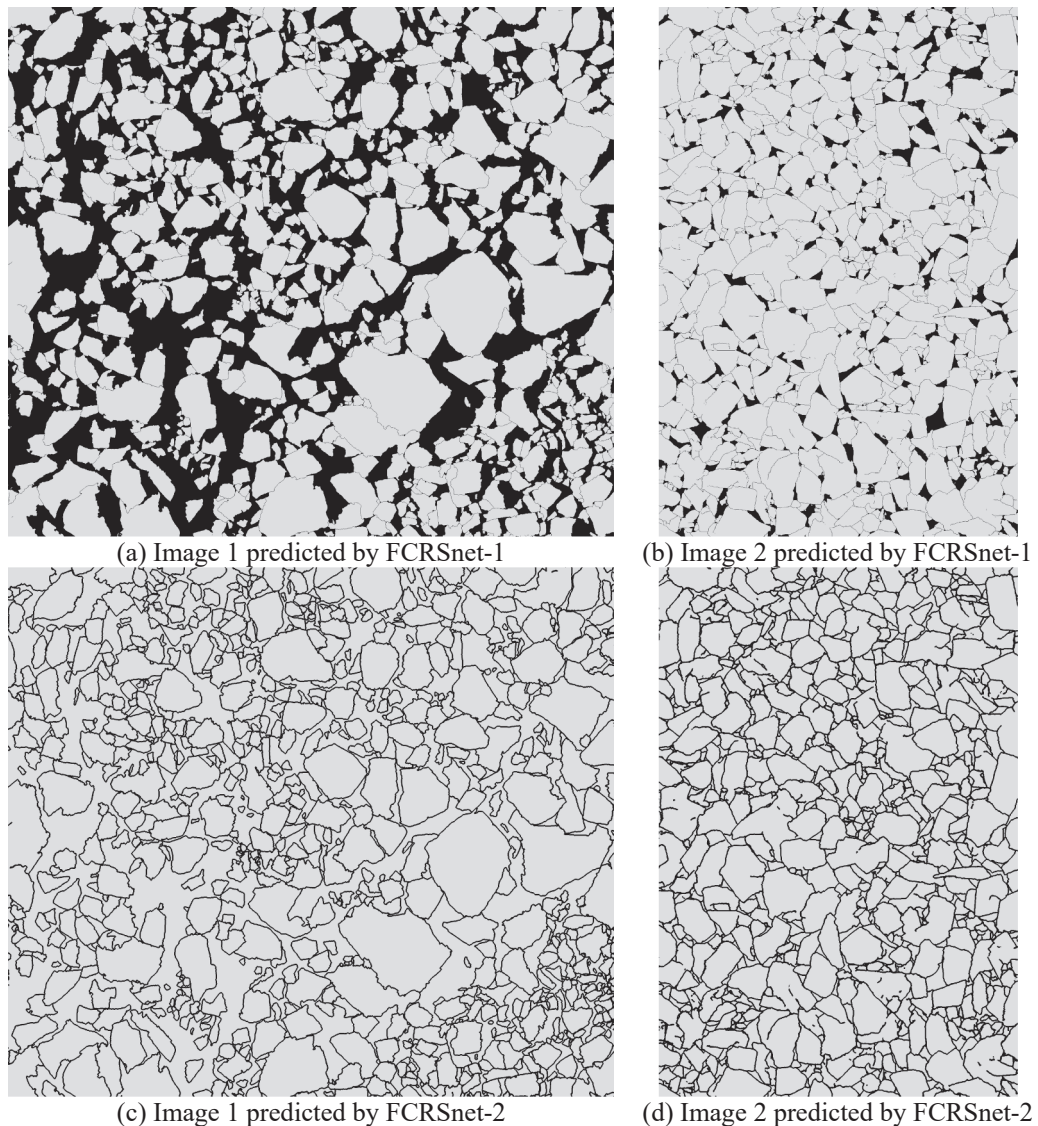


Fig. 11. Prediction results of FCRSnet-1 and FCRSnet-2.

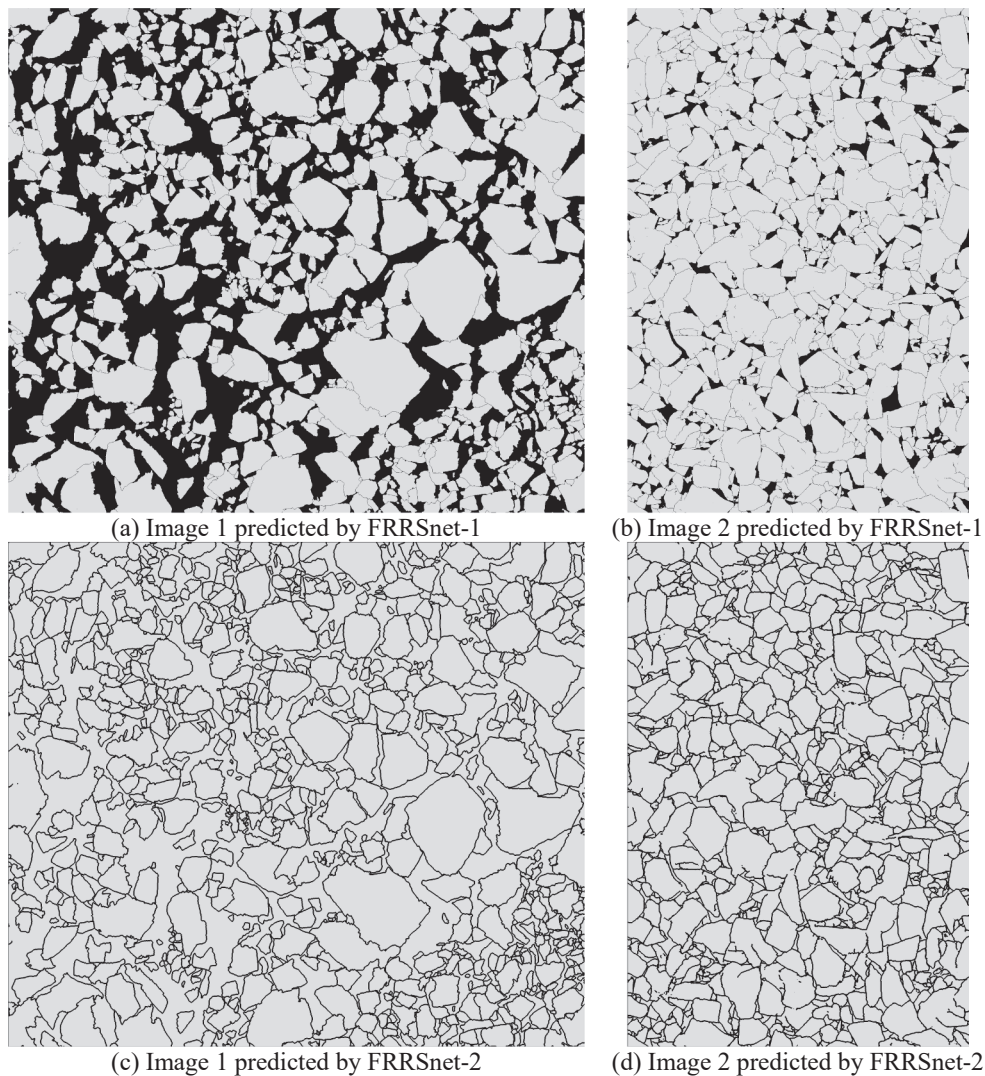


Fig. 12. Prediction results of FRRSnet-1 and FRRSnet-2.

output images of dataset-2, there are 317,779,535 black pixel points and 1,599,541,681 Gy pixel points, and the number of gray pixel points is 5.0335 times the number of black pixel points. Since the purpose of the second model is to obtain rock edges, the weight of black pixel points is set to 10 and the weight of gray pixel points is set to 1 when calculating the loss. Detailed training parameters are shown in [Table 1](#). The MIoU of each epoch during training is shown in [Fig. 10](#). The maximum MIoU during training is shown in [Table 1](#). The model size obtained after training is shown in [Table 1](#).

[Fig. 10](#) shows that FCRSnet has the strongest pre-learning capability compared to FRRSnet and FRRSnet+, indicating that skip architecture [39] can accelerate learning. As can be seen from [Table 1](#), compared to the basic network-48, the model size increases for both FCRSnet and FRRSnet+, while the model size of FRRSnet remains the same. For dataset-1, the learning ability of FRRSnet is optimal. And for dataset-2, the learning ability of FRRSnet+ is optimal. Combining dataset-1 and dataset-2, the learning ability of FRRSnet+ is optimal.

5.3. Model performance comparison

In step (2) of the model development process, this study obtained the prediction results of three models using FCRSnet-1, FRRSnet-1, and FRRSnet + -1 for dataset-2, respectively. Therefore, this study evaluates the performance of three models using MIoU and accuracy based on this

prediction results, as shown in [Table 2](#). Compared to the basic network-40, the MIoU and accuracy of FCRSnet increase by 0.77% and 0.25%, respectively, the MIoU and accuracy of FRRSnet increase by 1.47% and 0.47%, respectively, and the MIoU and accuracy of FRRSnet+ increase by 1.18% and 0.38%, respectively. It shows that the improved method of the basic network-40 in this study is feasible. Among the three models of FCRSnet-1, FRRSnet-1, and FRRSnet + -1, FRRSnet-1 has the best performance.

6. Experimental results and analysis

6.1. Prediction results and analysis

According to the application process of the BRPI segmentation method in [Fig. 8](#), test image 1 and test image 2 were predicted using the trained model, and the prediction results are shown in [Fig. 11](#), [Fig. 12](#), and [Fig. 13](#), respectively. The prediction results are evaluated using MIoU and accuracy, as shown in [Table 3](#).

From [Fig. 11\(a\)](#), [Fig. 12\(a\)](#), and [Fig. 13\(a\)](#), the predicted results of test image 1 have more edge discontinuity phenomena and fewer edge non-existence phenomena. It can be seen from [Fig. 11\(b\)](#), [Fig. 12\(b\)](#), and [Fig. 13\(b\)](#) that the predicted results of test image 2 have more phenomena of both edge discontinuity and edge non-existence. Comparing (a) and (c) in [Fig. 11](#), [Fig. 12](#), and [Fig. 13](#), respectively, there is almost no

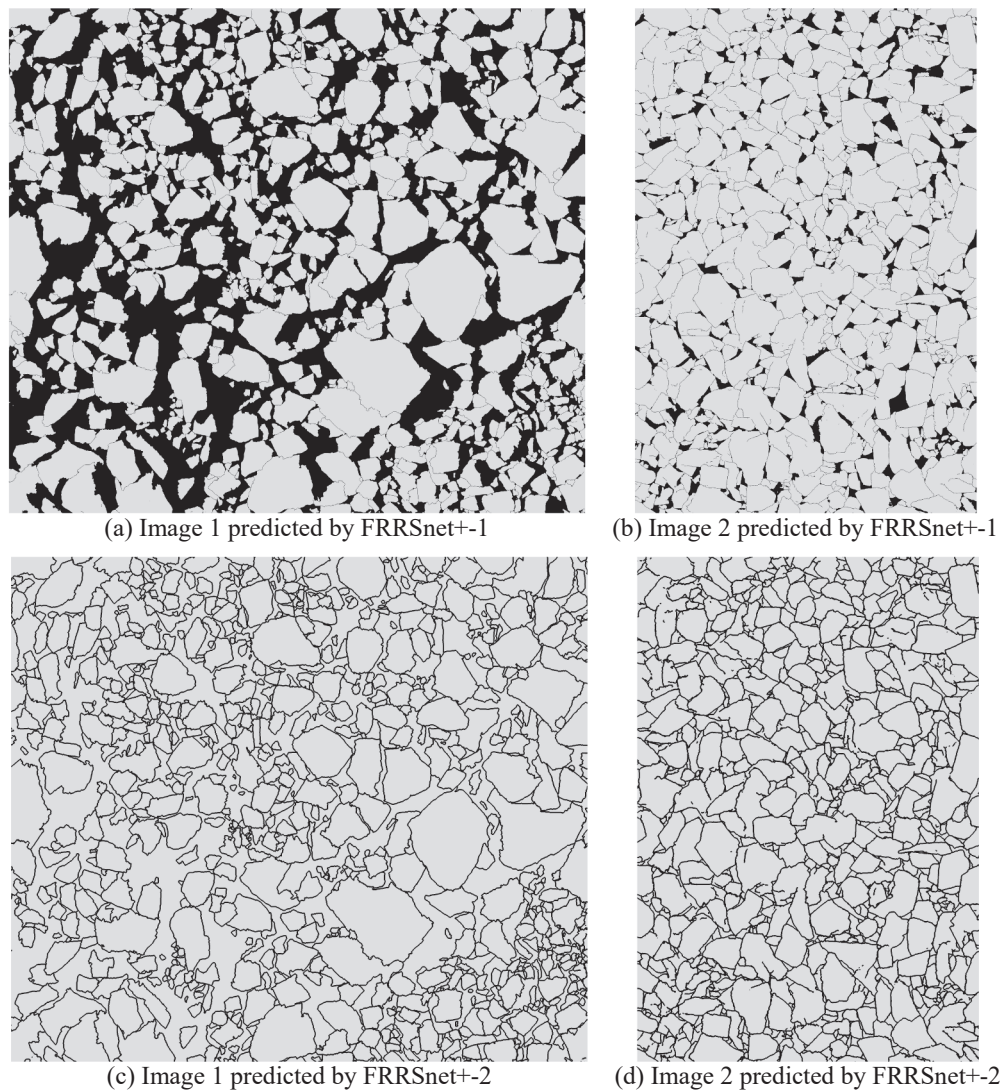


Fig. 13. Prediction results of FRRSnet + -1 and FRRSnet + -2.

Table 3
Model segmentation result evaluation indicators.

Indicator	FCRSnet		FRRSnet		FRRSnet+		
	1	2	1	2	1	2	
Image 1	MIoU(%)	99.19	97.51	99.53	98.28	99.45	98.65
	Accuracy(%)	99.64	99.39	99.79	99.58	99.75	99.67
Image 2	MIoU(%)	79.79	79.50	79.65	79.86	80.72	80.82
	Accuracy(%)	95.83	93.58	95.69	93.86	96.01	94.19
Total	MIoU (%)	95.17	89.51	95.25	90.16	95.54	90.79
	Accuracy(%)	98.16	97.14	98.19	97.37	98.30	97.55

edge discontinuity or non-existence in (c). From Fig. 11(d), Fig. 12(d), and Fig. 13(d), the predicted results of test image 2 have almost no edge discontinuity, but still have the phenomenon of edge non-existence. The above results show that the segmentation method proposed in this study can effectively solve the phenomenon of rock edge discontinuity and alleviate the problem of rock edge non-existent to a certain extent.

From Table 3, we can see that the prediction effect of test image 1 is much higher than that of test image 2, which is because the rock edge features of test image 1 are more obvious and easier to identify. Among the three models FCRSnet-1, FRRSnet-1, and FRRSnet + -1, FRRSnet-1 has the best prediction for test image 1 and FRRSnet + -1 has the best prediction for test image 2, indicating that FRRSnet + is more suitable

for predicting complex BRPI. Among the three models of FCRSnet-2, FRRSnet-2, and FRRSnet + -2, FRRSnet + -2 has the best prediction, indicating that FRRSnet + -2 is more suitable for extracting rock edges.

6.2. Analysis and comparison of BRPI segmentation results

The final segmentation results of test image 1 and test image 2 obtained using the segmentation method proposed in this study are shown in Fig. 14, Fig. 15, and Fig. 16. To demonstrate the necessity of the BRPI segmentation method proposed in this study, the results obtained using the segmentation method proposed in this study are compared with those obtained using FCRSnet-1, FRRSnet-1, and FRRSnet + -1. It should be noted that the predicted results of FCRSnet-1, FRRSnet-1, and FRRSnet + -1 have the more serious phenomenon of rock edge discontinuity or non-existence, which needs to be post-processed using the watershed algorithm, and the results are shown in Fig. 17.

From Fig. 14, Fig. 15, Fig. 16, and Fig. 17, it can be seen that the BRPI can all be more accurately segmented using semantic segmentation, but mis-segmentation is inevitable. To obtain the blasted rock fragment size cumulative distribution, the rocks are approximated as ellipses in this study. First, the area and perimeter of rock in the image are obtained using OpenCV, and the area and perimeter of rock are converted to the actual area and perimeter according to the ratio of the image to the real world. Then, the long and short axes of the ellipse are calculated based

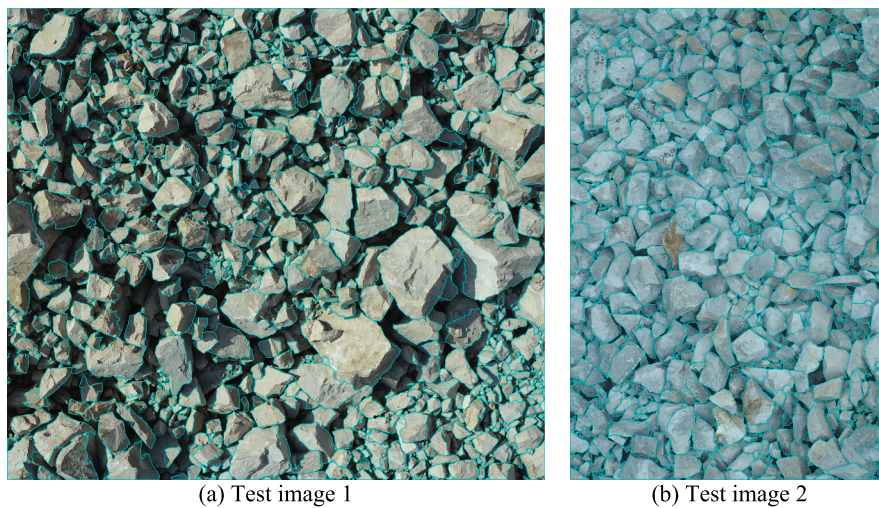


Fig. 14. The final segmentation results obtained using the FCRSnet-based segmentation method.

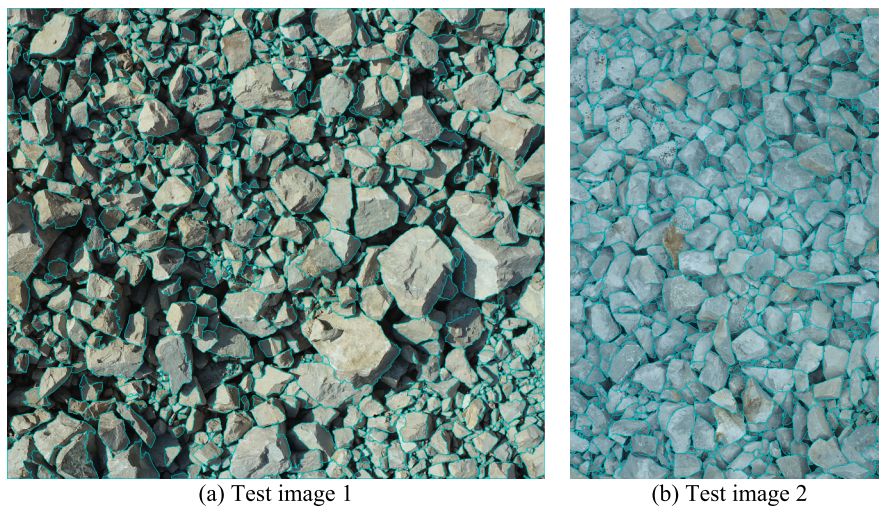


Fig. 15. The final segmentation results obtained using the FRRSnet-based segmentation method.

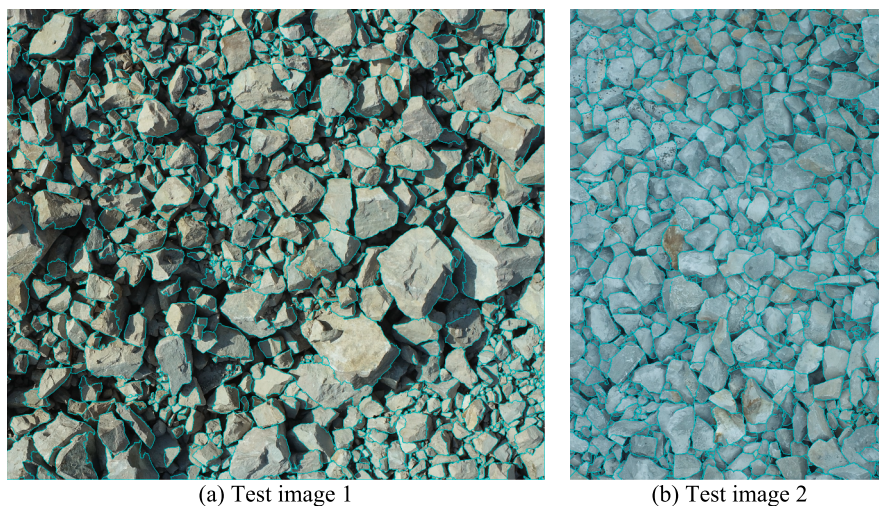


Fig. 16. The final segmentation results obtained using the FRRSnet + -based segmentation method.

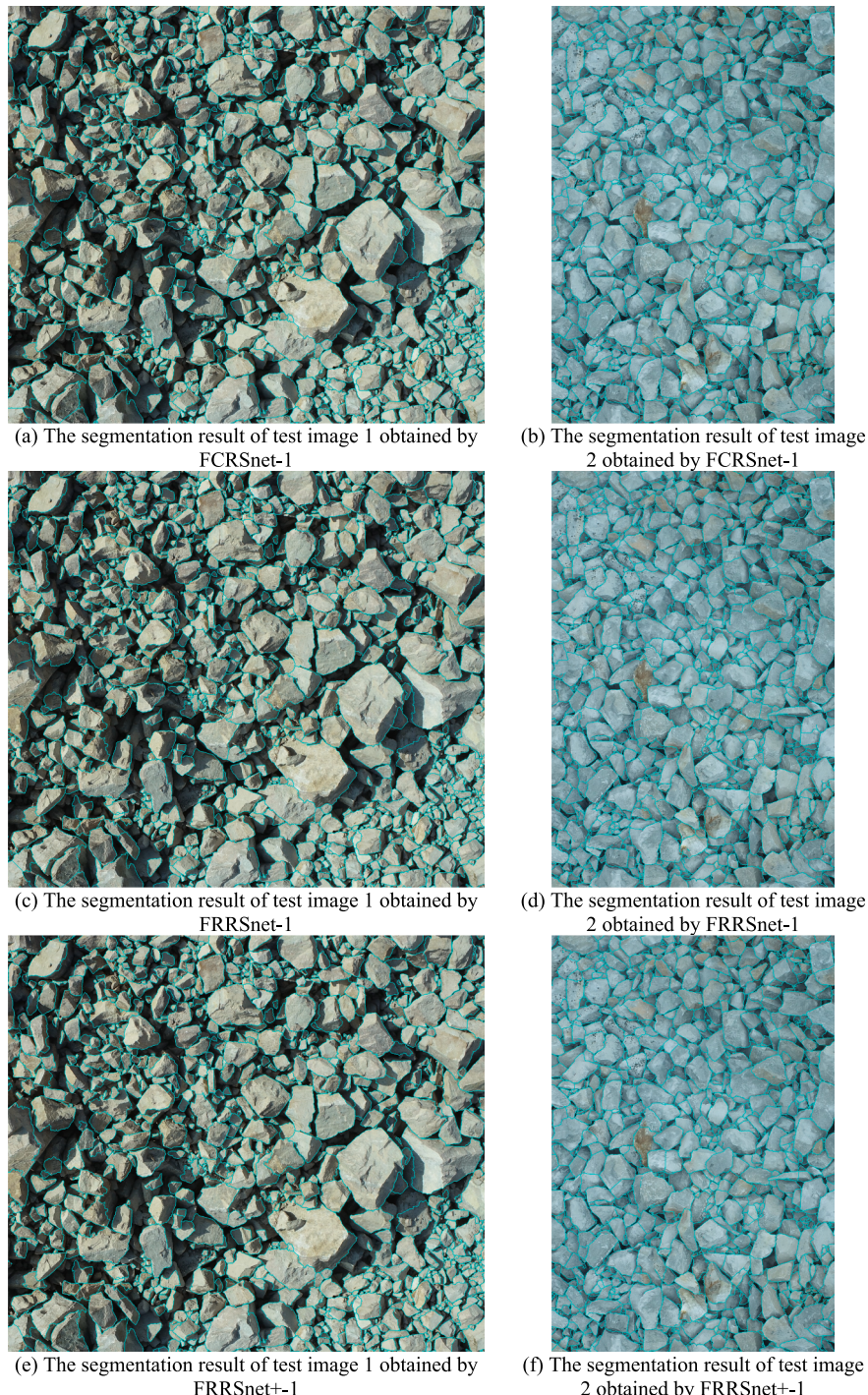


Fig. 17. The segmentation results obtained by FCRSnet-1, FRRSnet-1, or FRRSnet + -1.

on the area and perimeter, and the equivalent sieve size and volume of rock are calculated based on Equations (2) and (3) [40]. Finally, the blasted rock fragment size cumulative distribution is obtained according to Equation (4), and the distribution curves are shown in Fig. 18.

$$s = 1.16 \times b \times \sqrt{1.35 \times a/b} \quad (2)$$

$$v = \text{area} \times s \quad (3)$$

$$\text{Passing} = \frac{v}{v_{\text{total}}} \quad (4)$$

where a and b are the long and short axes of the approximate ellipse, s is

the equivalent sieve size, v is the equivalent sieve volume, Passing is the cumulative volume ratio of rocks, and v_{total} is the sum of equivalent sieve volumes of all rocks.

From Fig. 18, the distribution curves obtained by the above methods are all similar to the actual distribution curve, and the distribution curves of the test image 1 obtained using the segmentation method based on FRRSnet and the segmentation method based on FRRSnet + are almost completely overlapped with the real distribution curve. By comparing the distribution curves obtained by the BRPI segmentation method proposed in this study with those obtained using FCRSnet-1, FRRSnet-1, and FRRSnet + -1, the distribution curves obtained by the BRPI segmentation method proposed in this study are closer to the

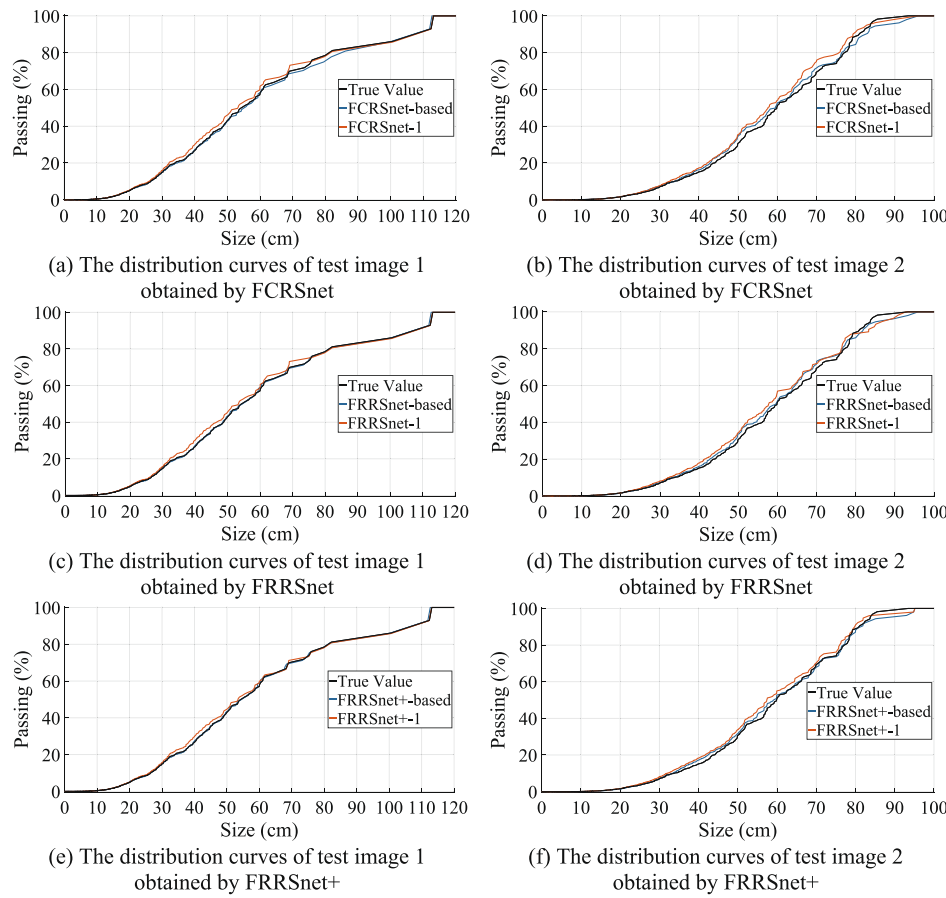


Fig. 18. Blasted rock fragment size cumulative distribution curves.

Table 4
10 characteristic sizes of test image 1.

Passing	100%	90%	80%	70%	60%	50%	40%	30%	20%	10%
True value (cm)	113.1	107.2	81.2	69.2	60.9	54.3	48.8	41.6	33.9	26.5
FCRSnet-based	Size (cm)	112.7	107.0	85.0	72.5	60.5	55.2	48.7	41.9	34.7
	RE (%)	0.43	0.26	4.66	4.76	0.58	1.60	0.22	0.81	2.09
FRRSnet -based	Size (cm)	112.7	107.1	81.3	70.3	60.4	54.5	48.5	41.8	34.0
	RE (%)	0.43	0.14	0.10	1.60	0.79	0.45	0.56	0.58	0.28
FRRSnet + -based	Size (cm)	112.7	107.1	81.2	70.3	60.4	54.5	48.5	41.8	33.9
	RE (%)	0.42	0.16	0.02	1.49	0.81	0.39	0.59	0.51	0.17
FCRSnet-1	Size (cm)	113.1	107.7	81.6	68.6	59.9	53.2	46.8	40.0	32.2
	RE (%)	0.07	0.40	0.48	0.95	1.60	1.97	3.96	3.71	5.20
FRRSnet-1	Size (cm)	113.1	107.7	81.7	68.6	60.0	53.3	46.6	39.9	32.2
	RE (%)	0.07	0.41	0.56	0.95	1.44	1.82	4.51	4.09	5.14
FRRSnet + -1	Size (cm)	113.1	107.6	81.5	69.0	60.1	53.4	47.0	40.1	32.2
	RE (%)	0.07	0.29	0.37	0.41	1.33	1.62	3.57	3.60	5.06
U-net	Size (cm)	112.9	107.4	81.6	68.8	59.6	53.0	45.2	39.7	31.9
	RE (%)	0.22	0.13	0.52	0.65	2.04	2.44	7.26	4.54	6.06
Segnet	Size (cm)	109.9	105.0	81.1	68.2	59.8	52.3	45.1	39.2	31.9
	RE (%)	2.9	2.07	0.2	1.56	1.8	3.68	7.45	5.59	5.88

actual distribution curve. To quantitatively evaluate obtained distribution curves, this study extracts 10 characteristic sizes from the distribution curves, which are important indicators to describe the cumulative distribution of blasted rock fragment sizes. Note that the characteristic sizes are blasted fragment sizes at $\text{Passing} = x\%$, and x is an integer multiple of 10. The characteristic sizes of test image 1 and test image 2 are shown in Table 4 and Table 5, respectively. The characteristic sizes were evaluated in this study using mean relative error (MRE), root mean square error ($RMSE$), and correlation coefficient (R^2), and the results are shown in Table 6.

As can be seen from Table 6, compared to FCRSnet-1, the MRE and $RMSE$ of the BRPI segmentation method based on FCRSNet are decreased by 1.04% and 0.28, respectively, and the R^2 is increased by 0.16%. Compared to FRRSnet-1, the MRE and $RMSE$ of the BRPI segmentation method based on FRRSnet are decreased by 1.54% and 0.72, respectively, and the R^2 is increased by 0.33%. Compared with FRRSnet + -1, the MRE and $RMSE$ of the BRPI segmentation method based on FRRSNet + decreased by 1.54% and 0.77%, respectively, and the R^2 increased by 0.31%. It shows that the segmentation method proposed in this study can effectively improve the segmentation accuracy of BRPI and reduce

Table 5

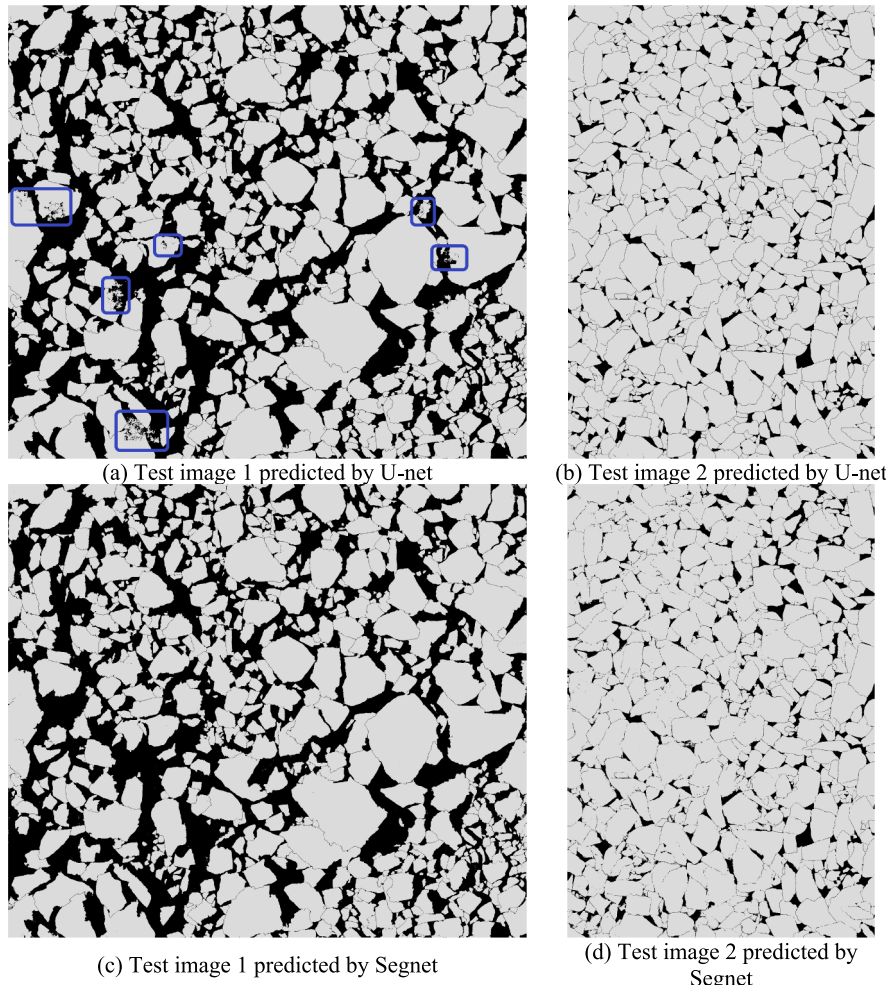
10 characteristic sizes of test image 2.

<i>Passing</i>		100%	90%	80%	70%	60%	50%	40%	30%	20%	10%
True value (cm)		93.4	80.9	77.1	70.4	65.9	59.9	56.1	49.9	43.9	33.7
FCRSnet-based	Size (cm)	96.0	82.5	76.5	69.2	64.2	59.5	53.4	48.5	42.9	33.8
	RE (%)	2.76	2.05	0.90	1.73	2.67	0.60	4.87	2.83	2.35	0.27
FRRSnet-based	Size (cm)	95.9	81.9	76.6	69.1	64.5	59.6	54.4	49.0	42.8	33.1
	RE (%)	2.73	1.23	0.70	1.82	2.15	0.42	3.17	1.66	2.58	1.82
FRRSnet + -based	Size (cm)	95.1	81.3	76.9	70.7	65.5	59.1	54.3	49.2	42.4	33.3
	RE (%)	1.89	0.56	0.36	0.40	0.65	1.25	3.27	1.40	3.35	1.18
FCRSnet-1	Size (cm)	95.9	79.3	75.8	66.8	63.7	57.6	51.9	48.0	42.1	32.6
	RE (%)	2.73	1.93	1.79	5.08	3.35	3.74	7.45	3.66	4.15	3.37
FRRSnet-1	Size (cm)	92.8	83.3	76.4	68.9	64.0	57.8	52.3	48.1	41.4	32.3
	RE (%)	0.60	3.02	1.01	2.21	2.93	3.48	6.80	3.65	5.67	4.22
FRRSnet + -1	Size (cm)	95.1	79.8	75.9	69.8	64.4	57.4	52.5	48.3	41.7	32.0
	RE (%)	1.89	1.34	1.56	0.83	2.33	4.13	6.48	3.07	5.01	5.19
U-net	Size (cm)	93.1	81.1	76.3	68.8	63.8	58.2	51.9	47.9	42.2	32.0
	RE (%)	0.26	0.29	1.09	2.29	3.3	2.75	7.55	3.96	3.83	4.96
Segnet	Size (cm)	92.6	81.3	76.3	68.8	63.6	57.4	51.9	47.9	41.9	32.1
	RE (%)	0.83	0.53	1.09	2.35	3.46	4.18	7.56	4.06	4.62	4.84

Table 6

Evaluation indicators.

Indicators	FCRSnet -based	FRRSnet -based	FRRSnet + -based	FCRSnet -1	FRRSnet -1	FRRSnet + -1	U-net	Segnet
MRE(%)	1.83	1.18	0.96	2.87	2.72	2.50	2.82	3.37
RMSE	1.61	0.97	0.78	1.89	1.69	1.55	1.77	2.12
R ² (%)	99.53	99.83	99.89	99.37	99.50	99.58	99.45	99.17

**Fig. 19.** The prediction results of comparison models.

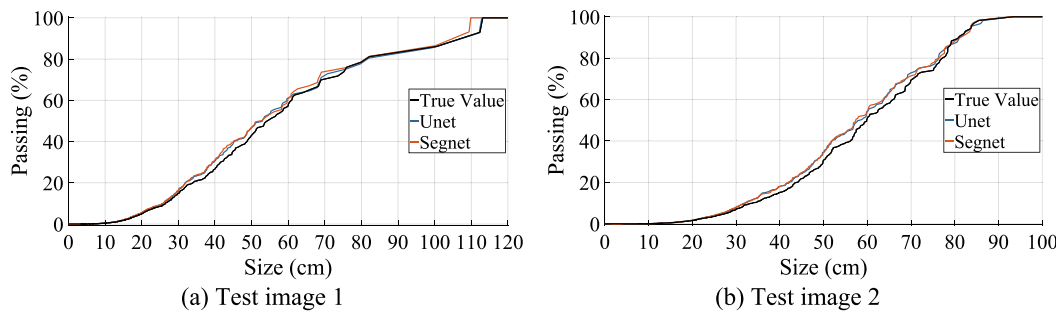


Fig. 20. Blasted rock fragment size cumulative distribution curves obtained by U-net and Segnet.

false segmentation. From **Table 6**, the *MRE*, *RMSE*, and *R²* evaluation indicators of the BRPI segmentation method based on FRRSnet + proposed in this study are optimal with 0.96%, 0.78 and 99.89%, respectively, indicating that the BRPI segmentation method based on FRRSnet + has the best segmentation effect.

6.3. Comparison with other methods

To demonstrate the superiority of the proposed network and segmentation method, the U-net [35] and Segnet [41] are used as comparison models for BRPI segmentation. The U-net and Segnet are written using the PyTorch 1.9.0 deep learning library in Python 3.8 language and trained using an RTX3090 GPU with 24 GB of video memory. The detailed training parameters of the model are shown in **Table 1**, and the MIoU of each epoch during model training is shown in **Fig. 10**. The comparison models are trained using 14,628 data. Then, the trained models are used for test images, and the prediction results are shown in **Fig. 19**. Finally, the segmentation results are obtained using the watershed algorithm, and **Fig. 20** shows the blasted rock fragment size cumulative distribution curves of the segmentation results. **Table 4** and **Table 5** show the characteristic sizes of the distribution curves. The evaluation indicators of the overall segmentation effect of comparison models are shown in **Table 6**.

As shown in **Table 1**, the U-net has the best training effect, but there is a problem in the prediction result of test image 1 obtained using the U-net, that is, the locations of misclassified pixels in the image are relatively concentrated, as shown in the blue boxes in **Fig. 19(a)**, indicating that the U-net may have overfitting phenomenon. Moreover, this error is unacceptable for rock segmentation. From **Fig. 19**, the U-net and Segnet are consistent with the networks proposed in this study, and their prediction results all have the problem of rock edge discontinuity or non-existence. As shown in **Table 1** and **Table 6**, the segmentation effect of the networks and segmentation method proposed in this study is better than the U-net and Segnet, and the network size of the U-net and Segnet is much larger than the networks proposed in this study.

7. Conclusions

In this study, a new deep learning network named FRRSnet + was proposed, and a BRPI segmentation method based on FRRSnet + was proposed to improve the accuracy of BRPI segmentation. The proposed FRRSnet + was formed by using skip architecture, identity mapping, and ASPP to improve the U-shaped network, which has the advantages of small model size and high segmentation accuracy. The proposed segmentation method was formed by combining FRRSnet+, watershed algorithm, and distance transformation. Through comprehensive analysis and verification, it is shown that the segmentation method can significantly improve the segmentation accuracy of BRPI, which proves the effectiveness and advancedness of the proposed segmentation method. The main conclusions of this study are as follows:

- (1). Compared with the skip architecture, identity mapping can increase the performance of network. Adding ASPP based on identity mapping can significantly improve the edge identification ability of the model.
- (2). Among the FCRSnet, FRRSnet, and FRRSnet+, the training and prediction results of FRRSnet + are superior. Moreover, although the model size of FRRSnet + is much smaller than that of U-net and Segnet, FRRSnet + can obtain better segmentation results than U-net and Segnet.
- (3). Among all the cumulative distribution curves of blasted rock fragment sizes obtained in this study, the BRPI segmentation method based on FRRSnet + has the best results. Moreover, the comparison shows that the segmentation method proposed in this study can effectively solve the phenomenon of rock edge discontinuity and alleviate the problem of rock edge non-existence to a certain extent.

CRediT authorship contribution statement

Qinpeng Guo: Investigation, Software, Data curation, Methodology, Validation, Writing – original draft. **Shijiao Yang:** Funding acquisition, Investigation, Supervision. **Yuchen Wang:** Data curation. **Huanbao Zhang:** Data curation.

Declaration of Competing Interest

The authors declare that they have no known competing financial interests or personal relationships that could have appeared to influence the work reported in this paper.

Data availability

Data will be made available on request.

Acknowledgements

The UAV and experimental sites from Guangdong Xiyuan Blasting Technology Co., Ltd are greatly appreciated. Financial support from Postgraduate Scientific Research Innovation Project of Hunan Province (No. QL20210216, No. QL20220211) are greatly appreciated.

Funding

This work was supported by Postgraduate Scientific Research Innovation Project of Hunan Province [grant numbers QL20210216, QL20220211]

References

- [1] E. Bakhtavar, R. Sadiq, K. Hewage, Optimization of blasting-associated costs in surface mines using risk-based probabilistic integer programming and firefly algorithm, *Nat. Resour. Res.* 30 (2021) 4789–4806, <https://doi.org/10.1007/s11053-021-09935-0>.

- [2] R. Bastami, A.A. Bazzazi, H.H. Shoormasti, K. Ahangari, Predicting and minimizing the blasting cost in limestone mines using a combination of gene expression programming and particle swarm optimization, *Arch. Min. Sci.* 65 (2020) 835–850, <https://doi.org/10.24425/ams.2020.135180>.
- [3] Y. Wang, Q. Guo, S. Yang, Z. Xiang, A prediction model for blasted block size grouping based on HC and RF-GA-BP neural network, *Arab. J. Geosci.* (2022) 1–15, <https://doi.org/10.1007/s12517-022-10645-x>.
- [4] P. Xu, R. Yang, J. Zuo, C. Ding, C. Chen, Y. Guo, S. Fang, Y. Zhang, Research progress of the fundamental theory and technology of rock blasting, *Int. J. Miner. Metall. Mater.* 29 (2022) 705–716, <https://doi.org/10.1007/s12613-022-2464-x>.
- [5] B. Dang, H. Nguyen-xuan, M. Abdel, An effective approach for VARANS-VOF modelling interactions of wave and perforated breakwater using gradient boosting decision tree algorithm, *Ocean Eng.* 268 (2023) 1–10, <https://doi.org/10.1016/j.oceaneng.2022.113398>.
- [6] L.V. Ho, T.T. Trinh, G. De Roeck, T. Bui-Tien, L. Nguyen-Ngoc, M. Abdel Wahab, An efficient stochastic-based coupled model for damage identification in plate structures, *Eng. Fail. Anal.* 131 (2022) 105866.
- [7] V. Tran, T. Nguyen, H. Nguyen-xuan, M. Abdel, Thin-Walled Structures Vibration and buckling optimization of functionally graded porous microplates using BCMO-ANN algorithm, *Thin-Walled Struct.* 182 (2023) 1–18, <https://doi.org/10.1016/j.tws.2022.110267>.
- [8] I.C. Engin, A practical method of bench blasting design for desired fragmentation based on digital image processing technique and Kuz-Ram model, in: FRAGBLAST9, 9th Int. Symp. Rock Fragm. by Blasting, 2010: pp. 257–263.
- [9] J.P. Latham, J. Kemeny, N. Maerz, M. Noy, J. Schleifer, S. Tose, A blind comparison between results of four image analysis systems using a photo-library of piles of sieved fragments, *Fragblast. 7* (2003) 105–132, <https://doi.org/10.1076/frag.7.2.105.15899>.
- [10] F. Siddiqui, S. Shah, M. Behan, Measurement of size distribution of blasted rock using digital image processing, *J. King Abdulaziz Univ. Sci.* 20 (2) (2009) 81–93.
- [11] A. Tosun, A modified Wipfrag program for determining muckpile fragmentation, *J. South. African Inst. Min. Metall.* 118 (2018) 1113–1119, <https://doi.org/10.17159/2411-9717/2018/v118n10a13>.
- [12] J.A. Sanchidrián, P. Segarra, F. Ouchterlony, L.M. López, On the accuracy of fragment size measurement by image analysis in combination with some distribution functions, *Rock Mech. Rock Eng.* 42 (2009) 95–116, <https://doi.org/10.1007/s00603-007-0161-8>.
- [13] J. Sudhakar, G.R. Adhikari, R.N. Gupta, Comparison of fragmentation measurements by photographic and image analysis techniques, *Rock Mech. Rock Eng.* 39 (2006) 159–168, <https://doi.org/10.1007/s00603-005-0044-9>.
- [14] M. Huang, Y. Liu, Y. Yang, Edge detection of ore and rock on the surface of explosion pile based on improved Canny operator, *Alexandria Eng. J.* 61 (2022) 10769–10777, <https://doi.org/10.1016/j.aej.2022.04.019>.
- [15] T. Bamford, K. Esmaeli, A.P. Schoellig, A real-time analysis of post-blast rock fragmentation using UAV technology, *Int. J. Mining, Reclam. Environ.* 0930 (2017) 1–18, <https://doi.org/10.1080/17480930.2017.1339170>.
- [16] Z. Yang, H. Ding, L.I. Guo, M. Lian, Superpixel image segmentation-based particle size distribution analysis of fragmented rock, *IEEE Access* 9 (2021) 59048–59058, <https://doi.org/10.1109/ACCESS.2021.3072998>.
- [17] M.J. Thurlay, Automated online measurement of limestone particle size distributions using 3D range data, *J. Process Control.* 21 (2011) 254–262, <https://doi.org/10.1016/j.jprocont.2010.11.011>.
- [18] Q. Guo, Y. Wang, S. Yang, Z. Xiang, A method of blasted rock image segmentation based on improved watershed algorithm, *Sci. Rep.* (2022) 1–21, <https://doi.org/10.1038/s41598-022-11351-0>.
- [19] Y. Lecun, Y. Bengio, G. Hinton, Deep learning, *Nature* 521 (2015) 436–444, <https://doi.org/10.1038/nature14539>.
- [20] K. Simonyan, Z. Andrew, Very deep convolutional networks for large-scale image recognition, *Comput. Sci.* (2014) 1–14.
- [21] B.A. Krizhevsky, I. Sutskever, G.E. Hinton, ImageNet classification with deep convolutional neural networks, *Adv. Neural Inf. Process. Syst.* 25 (2012).
- [22] D. Huong, M. Abdel, Advances in engineering software damage detection in slab structures based on two-dimensional curvature mode shape and faster R-CNN, *Adv. Eng. Softw.* 176 (2023) 1–12, <https://doi.org/10.1016/j.advengsoft.2022.103371>.
- [23] Z. Huang, J. Wang, X. Fu, T. Yu, Y. Guo, R. Wang, DC-SPP-YOLO: Dense connection and spatial pyramid pooling based YOLO for object detection, *Inf. Sci. (Ny)* 522 (2020) 241–258, <https://doi.org/10.1016/j.ins.2020.02.067>.
- [24] K. He, G. Georgia, P. Dollar, R. Girshick, R.-C.-N.-N. Mask, *IEEE Int. Conf. Comput. Vis.* 42 (2017) 2980–2988, <https://doi.org/10.1109/ICCV.2017.322>.
- [25] W. Qiao, Y. Zhao, Y. Xu, Y. Lei, Y. Wang, S. Yu, H. Li, Deep learning-based pixel-level rock fragment recognition during tunnel excavation using instance segmentation model, *Tunn. Undergr. Sp. Technol.* 115 (2021) 1–15, <https://doi.org/10.1016/j.tust.2021.104072>.
- [26] X. Zhou, Q. Gong, Y. Liu, L. Yin, Automatic segmentation of TBM muck images via a deep-learning approach to estimate the size and shape of rock chips, *Autom. Constr.* 126 (2021) 1–20, <https://doi.org/10.1016/j.autcon.2021.103685>.
- [27] P. Loncomilla, P. Samtani, J. Ruiz-del-Solar, Detecting rocks in challenging mining environments using convolutional neural networks and ellipses as an alternative to bounding boxes, *Expert Syst. Appl.* 194 (2022), 116537, <https://doi.org/10.1016/j.eswa.2022.116537>.
- [28] A. Garcia-Garcia, S. Orts-Escalano, S. Oprea, V. Villena-Martinez, P. Martinez-Gonzalez, J. Garcia-Rodriguez, A survey on deep learning techniques for image and video semantic segmentation, *Appl. Soft Comput. J.* 70 (2018) 41–65, <https://doi.org/10.1016/j.asoc.2018.05.018>.
- [29] H. Li, G. Asbjörnsson, M. Lindqvist, Image process of rock size distribution using densenet-based neural network, *Minerals* 11 (2021) 1–13, <https://doi.org/10.3390/min11070736>.
- [30] X. Liu, Y. Zhang, H. Jing, L. Wang, S. Zhao, Ore image segmentation method using U-Net and Res_Unet convolutional networks, *RSC Adv.* 10 (2020) 9396–9406, <https://doi.org/10.1039/c9ra05877j>.
- [31] H. Li, C. Pan, Z. Chen, A. Wulamu, A. Yang, Ore image segmentation method based on u-net and watershed, *Comput. Mater. Contin.* 65 (2020) 563–578, <https://doi.org/10.32604/cmc.2020.09806>.
- [32] S. Minaee, Y. Boykov, F. Porikli, A. Plaza, N. Kehtarnavaz, D. Terzopoulos, Image segmentation using deep learning: a survey, *IEEE Trans. Pattern Anal. Mach. Intell.* 44 (2022) 3523–3542, <https://doi.org/10.1109/TPAMI.2021.3059968>.
- [33] F. Schenk, A. Tscharf, G. Mayer, F. Fraundorfer, Automatic muck pile characterization from UAV images, *ISPRS Ann. Photogramm. Remote Sens. Spat. Inf. Sci. IV-2/W5* (2019) 163–170, <https://doi.org/10.5194/isprs-annals-IV-2-W5-163-2019>.
- [34] S. Shrivastava, D. Deb, S. Bhattacharjee, Prediction of particle size distribution curves of dump materials using convolutional neural networks, *Rock Mech. Rock Eng.* 55 (2022) 471–479, <https://doi.org/10.1007/s00603-021-02657-y>.
- [35] O. Ronneberger, P. Fischer, T. Brox, U-Net: Convolutional Networks for Biomedical Image Segmentation, in: *Med. Image Comput. Comput. Interv. – MICCAI 2015*, 2015: pp. 234–241. https://doi.org/10.1007/978-3-319-24574-4_28.
- [36] K. He, X. Zhang, S. Ren, J. Sun, Deep Residual Learning for Image Recognition, 2016 *IEEE Conf. Comput. Vis. Pattern Recognit.* (2016) 770–778, <https://doi.org/10.1109/CVPR.2016.90>.
- [37] L.C. Chen, Y. Zhu, G. Papandreou, F. Schroff, Encoder-decoder with atrous separable convolution for semantic image segmentation, *Comput. Vis. – ECCV 2018 (11211)* (2018) 1–18, https://doi.org/10.1007/978-3-030-01234-2_49.
- [38] K. He, X. Zhang, S. Ren, J. Sun, Delving deep into rectifiers: surpassing human-level performance on imagenet classification, *Proc. IEEE Int. Conf. Comput. Vis.* (2015) 1026–1034, <https://doi.org/10.1109/ICCV.2015.123>.
- [39] E. Shelhamer, J. Long, T. Darrell, Fully convolutional networks for semantic segmentation, *IEEE Trans. Pattern Anal. Mach. Intell.* 39 (2017) 640–651, <https://doi.org/10.1109/TPAMI.2016.2572683>.
- [40] A.J. Hardy, T.M. Ryan, J.M. Kemeny, Block size distribution of in situ rock masses using digital image processing of drill core, *Int. J. Rock Mech. Min. Sci. Geomech. Abstr.* 34 (1997) 303–307, [https://doi.org/10.1016/S0148-9062\(96\)00058-7](https://doi.org/10.1016/S0148-9062(96)00058-7).
- [41] V. Badrinarayanan, A. Kendall, R. Cipolla, S. Member, SegNet : a deep convolutional encoder-decoder architecture for image segmentation, *IEEE Trans. Pattern Anal. Mach. Intell.* (2017), <https://doi.org/10.1109/TPAMI.2016.2644615>.